Nanobeam Mechanics: Elasticity, Strength, and Toughness of Nanorods and Nanotubes

Eric W. Wong,* Paul E. Sheehan,* Charles M. Lieber†

The Young's modulus, strength, and toughness of nanostructures are important to proposed applications ranging from nanocomposites to probe microscopy, yet there is little direct knowledge of these key mechanical properties. Atomic force microscopy was used to determine the mechanical properties of individual, structurally isolated silicon carbide (SiC) nanorods (NRs) and multiwall carbon nanotubes (MWNTs) that were pinned at one end to molybdenum disulfide surfaces. The bending force was measured versus displacement along the unpinned lengths. The MWNTs were about two times as stiff as the SiC NRs. Continued bending of the SiC NRs ultimately led to fracture, whereas the MWNTs exhibited an interesting elastic buckling process. The strengths of the SiC NRs were substantially greater than those found previously for larger SiC structures, and they approach theoretical values. Because of buckling, the ultimate strengths of the stiffer MWNTs were less than those of the SiC NRs, although the MWNTs represent a uniquely tough, energy-absorbing material.

The mechanical properties of small, rod-like materials are of considerable interest. For example, small whiskers can have strengths considerably greater than those observed in corresponding macroscopic single crystals (1–3), an effect that is attributed to a reduction in the number of defects per unit length (compared with larger structures) that lead to mechanical failure. Systematic increases in strength with decreasing whisker diameters in the 100- to 1-μm regime clearly support this idea (4, 5). It is also true that the maximum strengths of the best whisker materials, such as SiC, still fall below the theoretically predicted values (4, 6, 7). It is thus reasonable to consider whether NRs and nanotubes will exhibit greater strengths than previously observed in micrometer-diameter whiskers and, furthermore, whether these nanoscale materials will exhibit new phenomena. For example, recent simulations and transmission electron microscope (TEM) observations have indicated that carbon nanotubes elastically buckle (versus fracture or plastically deform) when bent to large angles (8–13).

Until recently, the lack of nanowhiskers and mechanical measurement techniques applicable to these materials has precluded addressing the key issues given above. The development of synthetic methods for preparing carbon nanotubes (11, 14, 15), carbide NRs (16), and oxide NRs (17) has now provided a wide range

E. W. Wong and P. E. Sheehan, Department of Chemistry, Harvard University, Cambridge, MA 02138, USA.
C. M. Lieber, Department of Chemistry and Division of Engineering and Applied Sciences, Harvard University, Cambridge, MA 02138, USA.

*Both authors contributed equally to this work.
†To whom correspondence should be addressed. E-mail: cml@cmliris.harvard.edu

of nanoscale whisker materials. Carbon nanotubes and SiC NRs (16) are particularly interesting because micrometer-sized carbon fibers and SiC whiskers are widely used to strengthen composite materials. However, the rational design of new composites requires a clear understanding of the stiffness, strength, and toughness of these nanosized tubes and rods.

Previous mechanical studies of whiskers have been performed by mounting the two ends of a single whisker in an apparatus that bends or pulls the whisker with a controllable force. This approach has worked well for whiskers with diameters ≥10 μm but has been much less reliable for whiskers with smaller diameters (6, 18). The difficulties in mounting even micrometer-diameter materials suggest that new approaches are needed to probe the mechanics of NRs and nanotubes. One recent method (19, 20) has measured the amplitude of thermally excited vibrations in a TEM. Analysis of the temperature dependence of the vibration amplitude gives an estimate of the Young's modulus (E), a measure of stiffness. This technique is limited in several important ways. First, the thermally excited vibrations must be neither too large nor too small for reliable TEM detection, thus restricting the size (diameter and length) of samples. Second, this approach cannot evaluate the strength and toughness of NRs and nanotubes, even though these properties are critical to applications. Here, we report a method that enables the direct determination of the bending force as a function of displacement. This technique can be used to clearly elucidate the mechanics of whiskerlike materials in the nanometer- through micrometer-sized regime and, as shown below, provides an unambiguous measure of the stiffness, strength, and toughness of SiC NRs and carbon nanotubes.

To determine directly the force versus displacement (F-d) characteristics of a rod requires that two connections be made to it. One of these may be fixed, but the other connection must permit measurement of F and d. Making two connections on such a small scale is inherently difficult; however, in recent studies of the electrical conductivity of carbon nanotubes, we devised a flexible method that uses conventional lithography to pin one end of the nanostructure and an atomic force microscope (AFM) to locate and probe the regions protruding from the static contact (21). Here, we used this same basic approach. First, NRs or nanotubes were dispersed randomly on a flat surface and then pinned to this substrate by deposition of a regular array of square pads. The AFM was used to directly measure lateral F-d characteristics at varying distances from the pinning point (Fig. 1).

Single-crystal MoS_2 was used as the substrate in these experiments, because it has a low coefficient of friction and may be cleaved to produce large, atomically flat surfaces (22). We pinned NRs and nanotubes to this flat surface by depositing pads of a rigid oxide, SiO, through a shadow mask (Fig. 1, A and B). The AFM was then used to locate and characterize the dimensions of protruding rods or tubes (21). A representative image of a pinned, 35.3-nm-diameter SiC NR (Fig. 1C) shows that the model structure (Fig. 1A) is readily achieved experimentally.

Lateral F-d curves were recorded at different positions along the length of the nanobeam (that is, the NR or nanotube) (Fig. 1D). Before contact, a small, ≤1-nN lateral (friction) force was observed as the tip was scanned perpendicular to the axis of the nanobeam. After contact, the measured lateral force increased linearly as the nanobeam was elastically displaced from its equilibrium position; the AFM tip remained on the MoS_2 surface during this deflection process. It is possible at large displacements to fracture or plastically deform a nanobeam and thereby determine its strength. Alternatively, the tip can move over the deflected structure when the applied normal load is small (23), and, thus, it is possible to deform the beam controllably without damage. In this way, we measured F-d curves repeatedly at many points along a nanobeam.

The F-d data acquired in this way were used to determine the E of a nanobeam. For our experimental geometry (Fig. 1E), the general response of a beam to a force P applied at a distance a (along the x axis) from the fixed pinning point (x = 0) is given by (24)

$$EI \frac{d^4y}{dx^4} = -f + P\delta(x - a) \qquad (1)$$

where I is the moment of inertia of the beam and f is a beam-surface friction force opposing P. This equation can be integrated and rearranged to express the applied force in terms of the Young's modulus and displacement y (25):

$$P(x,y) = 3EI \frac{y}{x^3} + \frac{f}{8}\left(x - 4L - 6\frac{L^2}{x}\right) \quad (2)$$

where L is the length of the exposed nanobeam. The friction force f is quite small in these experiments, and its contribution can be eliminated entirely by analysis of the nanobeam force constant, $k(x) = dP/dy$:

$$k(x) = \frac{3\pi r^4}{4x^3} E \qquad (3)$$

where $\pi r^4/4$ is I for a solid cylinder of radius r. Because we determine $k(x)$ for many values of x in these experiments, it is possible to obtain a reliable measure of E without knowledge of the exact point where a nanobeam is pinned (26).
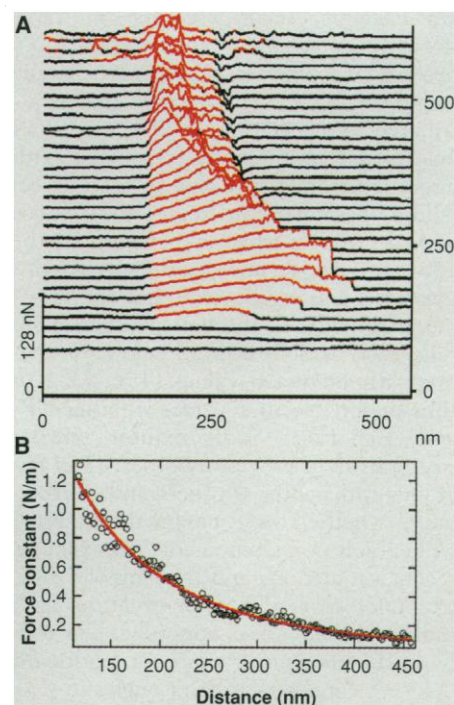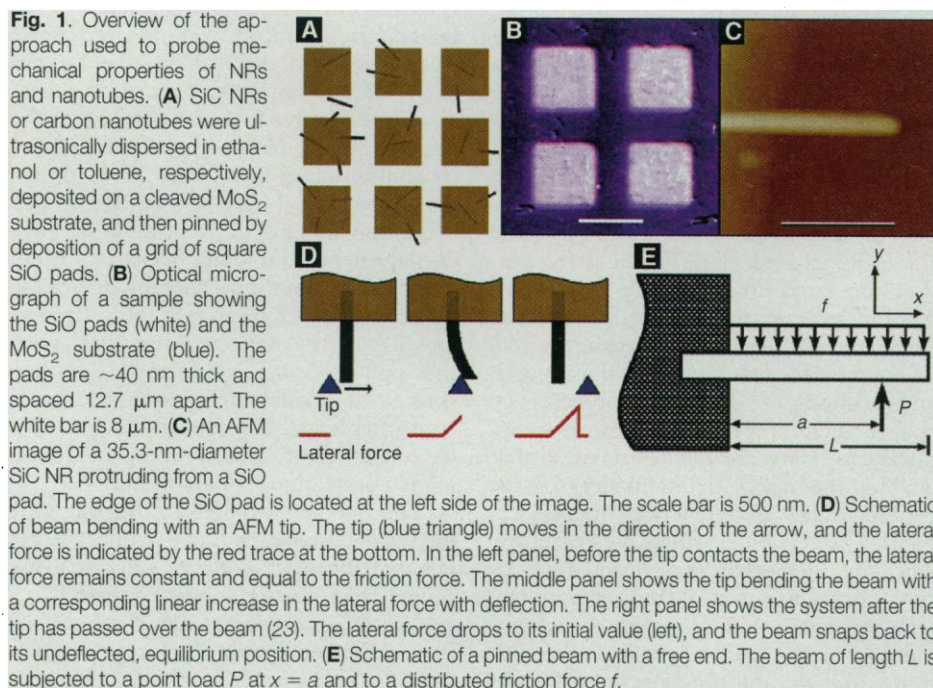
The mechanical properties of large (≥ 1 μm) SiC structures have been extensively studied and thus can serve as a useful reference point for our nanoscale measurements. In particular, it is expected that the E values of the NRs should be comparable with the values determined previously in larger structures, because elastic deformations are determined by the chemical bonding (27). A typical plot of the F-d data recorded on an 23.0-nm-diameter SiC NR is presented as an image (Fig. 2A). The scans were

recorded rastering the sample from right to left; a total of ~300 individual scans were recorded at different distances along the NR, although only 29 are shown for clarity. These data illustrate several important points. First, the initial location at which the lateral F begins to increase in each horizontal scan is about the same. This result indicates that the NR returns to the same equilibrium position after being released by the tip. We can therefore conclude that (i) the NR deflection is elastic, (ii) the NR-surface friction force is small compared with the NR restoring force, and (iii) the portion of the NR under the pinning pad does not move (28). Second, the lateral force recorded in each of the individual scans increases linearly once the tip makes contact with the NR; that is, $P = ky$. Third, the slopes of the F-d scans, k, decrease for scan lines recorded at increasingly large distances from the NR pinning point at the top of Fig. 2A. These two latter points agree qualitatively with the behavior outlined in Eqs. 2 and 3.

We can calculate E from any single F-d curve using Eq. 3, although we used the full set of curves acquired as a function of position because they provide a more robust determination. A typical plot of $k(x)$ versus x from these data (Fig. 2B) shows that $k(x)$ decreases nonlinearly with x and that this decrease is well fit to the $1/x^3$ dependence (coefficients of correlation ≥ 0.96 in all data sets) predicted by Eq. 3. Fitting the data in Fig. 2B yielded an E of 610 GPa. In comparison, the E obtained from data recorded on a 21.5-nm-diameter SiC NR was 660 GPa. These results agree well with the

600-GPa value predicted theoretically for [111]-oriented SiC (29) and the average values obtained previously for micrometer-diameter whiskers (6).

Similar measurements were made on multiwall carbon nanotubes (MWNTs) prepared by arc discharge (11, 14). The straight nanotubes produced by this method have a relatively low density of defects and contain well-ordered concentric graphene shells. A typical image of the F-d data recorded on a 32.9-nm-diameter MWNT is shown in Fig. 3A. These F-d data exhibit features similar to those described above for the SiC NRs. In particular, there was a linear increase in F with d after the tip contacted the nanotube, and the slope of this linear region decreased for data recorded at increasing distance from the pinning point (30). The value of E determined from fits to Eq. 3 (Fig. 3B) was 1.26 TPa (31). Similar results were obtained from the analysis of F-d data acquired on six dif-

Fig. 1. Overview of the approach used to probe mechanical properties of NRs and nanotubes. (**A**) SiC NRs or carbon nanotubes were ultrasonically dispersed in ethanol or toluene, respectively, deposited on a cleaved MoS_2 substrate, and then pinned by deposition of a grid of square SiO pads. (**B**) Optical micrograph of a sample showing the SiO pads (white) and the MoS_2 substrate (blue). The pads are ~40 nm thick and spaced 12.7 μm apart. The white bar is 8 μm. (**C**) An AFM image of a 35.3-nm-diameter SiC NR protruding from a SiO pad. The edge of the SiO pad is located at the left side of the image. The scale bar is 500 nm. (**D**) Schematic of beam bending with an AFM tip. The tip (blue triangle) moves in the direction of the arrow, and the lateral force is indicated by the red trace at the bottom. In the left panel, before the tip contacts the beam, the lateral force remains constant and equal to the friction force. The middle panel shows the tip bending the beam with a corresponding linear increase in the lateral force with deflection. The right panel shows the system after the tip has passed over the beam (23). The lateral force drops to its initial value (left), and the beam snaps back to its undeflected, equilibrium position. (**E**) Schematic of a pinned beam with a free end. The beam of length L is subjected to a point load P at $x = a$ and to a distributed friction force f.

ferent MWNTs with diameters from 26 to 76 nm: The average E value from these experiments was 1.28 ± 0.59 TPa with no dependence on tube diameter. The MWNT E value was about two times that of our SiC NRs and similar to the in-plane modulus of graphite, 1.06 TPa (32); the in-plane modulus of graphite is the largest of any known bulk material.

These measured values of E may be compared with a recent experimental study (19) and theoretical estimates for carbon nanotubes (8, 10, 33–36). The E values of MWNTs have been estimated from the analysis of thermally excited vibrations measured in a TEM (19). The average value determined in this study, 1.8 TPa, is somewhat greater than our 1.28-TPa average, although the large uncertainty in this previous measurement, ± 1.4 TPa, makes these two independent determinations statistically indistinguishable. Our experimental results are also consistent with several theoretical estimates that indicate that E should be comparable with the 1.06-TPa in-plane modulus of graphite (33, 35, 36). However,

other computational work has suggested a substantially larger E for single-wall nanotubes (SWNTs) (8, 10, 34). We believe that this difference is due to the choice of wall thickness used to calculate E and not to the small tube diameters investigated in these latter studies. Hence, it will be interesting to experimentally probe the diameter dependence of E in SWNTs as these materials become available.

In addition, our nanotube F-d data exhibit new features that have important implications for applications. Specifically, MWNTs can be elastically deflected to a much greater extent than SiC NRs (Fig. 3), and the F-d curves deviate substantially from the single linear slope predicted for simple beam bending (Fig. 4). The initial linear slope in F-d plots decreased abruptly when the nanotubes were deflected by relatively large amounts. From all of our measurements, we found that this abrupt decrease occurs at a deflection angle of about 10° for $x \approx 1$ μm (37). A comparison of two curves recorded 2.7 nm apart along a nanotube axis (Fig. 4A) shows nearly identical F-d behavior and thus strongly suggests that the abrupt change in slope corresponds to an elastic process; that is, energy is not dissipated in bond breaking or rearrangement. Notably, this behavior deviates from that reported in previous mechanical de-

flection studies of whiskers (4, 5, 38) and that found for our SiC NRs. This behavior does, however, agree qualitatively with recent simulations suggesting that single- and double-wall nanotubes buckle elastically to yield a structure reminiscent of that formed when a macroscopic rubber tube is bent and kinked (8, 9).

We believe that the discontinuities in our F-d curves on MWNTs correspond to the elastic buckling found in simulations (37). Strong evidence for this conclusion was obtained in direct bending experiments in which high-friction substrates were used to trap nanotubes in highly deflected configurations (Fig. 5A). Importantly, these images exhibit a beadlike structure (not seen in the straight tubes) that is consistent with the expected height increases at the buckling points. In addition, buckled nanotubes have been observed in TEM images (9, 12) and have been found to result from support-induced strain (13).

Although buckling provides a reasonable explanation for the discontinuity in our F-d data, a detailed comparison of the changes in force and strain energy at the buckling point with simulations shows important differences (8). The simulation predicts that there is about a 30% drop in the force after buckling and that further dis-
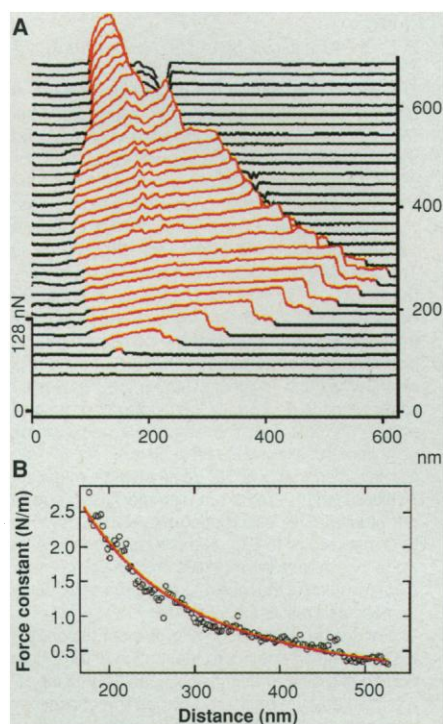

Fig. 3. (A) Surface plot showing the F-d response of a 32.9-nm-diameter MWNT recorded with a normal load of 16.4 nN. The image is tilted 30° and displays only 30 of the ~300 F-d traces in the original image for clarity. The nanotube is pinned by a SiO pad beyond the top of the image. The data were recorded in water to minimize the nanotube-MoS$_2$ friction force. **(B)** Dependence of force constant on position x along the axis of the same nanotube. The carbon nanotubes used in these studies were purified by oxidation to 5% of the initial sample.
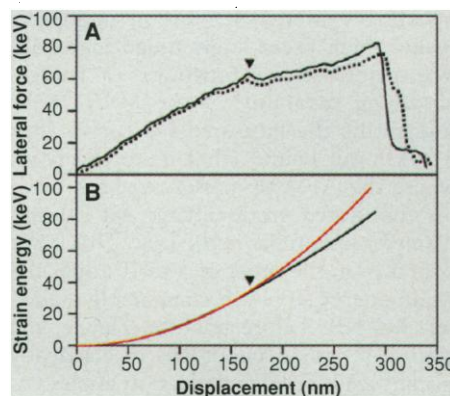

Fig. 4. (A) Two consecutive lateral force traces for a 32.9-nm-diameter MWNT. The dashed curve was recorded at a distance 2.7 nm down the nanotube from the solid curve; the solid curve was recorded 813 nm from the pinning point. In both traces, the lateral force increases linearly up to the point marked with an inverted black triangle; after this point, there is a small drop in restoring force followed by an increase with continued displacement. The large decrease in force at the ends of these traces corresponds to the point at which the tip moves over the nanotube. **(B)** The strain energy corresponding to the solid trace in (A) (solid black curve). The solid red curve was obtained from a quadratic fit to the region before the buckling point (inverted black triangle). After the buckling point, the experimental strain energy increases more slowly than expected for a harmonic system.
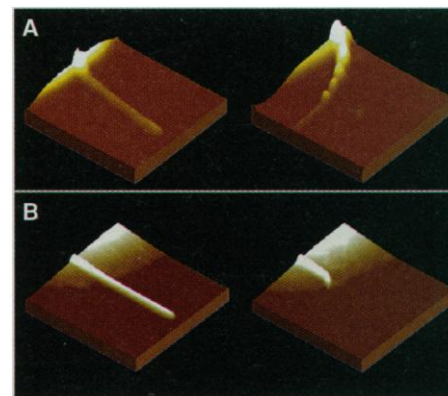

Fig. 5. (A) Images (0.9 μm by 0.9 μm) of a 4.4-nm-diameter MWNT before and after bending on an oxidized silicon substrate. The left image shows the nanotube, which was pinned by a SiO pad at the left side, in its equilibrium position. The nanotube was then bent by scanning with the tip in contact with the surface. The right image shows bumps along the nanotube that correspond to positions at which buckling occurs. Both images were recorded in tapping mode to minimize the applied lateral forces. **(B)** Images (1.25 μm by 1.25 μm) of a 21.5-nm-diameter SiC NR before and after bending on a MoS$_2$ substrate. The left image shows the NR, which was pinned by a SiO pad at the left side, in its equilibrium position. Application of a high lateral load resulted in the fracture of the NR. The right image of the fractured NR shows that the NR broke at the pinning site ($x = 0$).

placement occurs at nearly constant force. Correspondingly, the strain energy shows a crossover from quadratic (harmonic) to linear dependence after buckling. Our measurements exhibit only a small drop in force after buckling and an increasing, albeit smaller, F-d result for continued deflection. Integration of the force data shows that the strain energy deviates substantially from the quadratic dependence after the assigned buckling point, although the dependence is nonlinear (Fig. 4B). There are several possible explanations for the differences between our experiments and simulations. First, the present experiments were carried out on MWNTs, whereas the simulated strain energy and F-d results were for small (that is, 1-nm diameter by 8-nm length) SWNTs. It is possible that adjacent tubes in multiwall samples exhibit some relative slippage or buckle (or both) at slightly differing strains during bending and thus broaden the discontinuity compared with SWNTs. Second, it is possible that the potential used in simulations is not sufficient to describe the behavior at large deformations well. Because this discrepancy has important implications for applications such as composites, we believe that it will be important to resolve through further experiments on SWNTs (15) and analyses of simulations.

The large E values determined for MWNTs and SiC NRs make these materials obvious candidates for the reinforcing element in ceramic, metal, and polymer matrix composites. Although many other factors must be considered in making a useful composite (39), at least the strength and toughness of the nanotubes and NRs should be quantified, because they place limits on the potential composite properties. Strength and toughness refer to the maximum force per unit area and the elastic energy stored or absorbed by a material before failure, respectively. To the best of our knowledge, these critical properties have not been measured previously for carbon nanotubes or carbide NRs. The bending strength for SiC NRs is determined from the maximum strain (at the pinning site) just before fracture (Fig. 5B), and for the MWNTs the bending strength is defined as the strain determined at the initial buckling point. The buckling point is taken as a measure of the bend strength, because the stiffness drops substantially at this point and would likely lead to failure in a rigid composite (40).

The maximum bending strength determined for MWNTs examined in this study was 28.5 GPa; however, the average value was considerably smaller: 14.2 ± 8.0 GPa. In contrast, the largest SiC NR strength observed, 53.4 GPa, is substantially larger than the nanotubes values and approaches the predicted maximum of $0.1E$ (7). This strength value is also two times the best

previously observed value in micrometer-diameter whiskers (6). The greatest strengths were found for NRs that fractured at the pinning site where the strain was greatest (Fig. 5B), whereas lower values were found for SiC NRs that fractured some distance from the pinning site. These observations clearly suggest that defects can limit the strengths of the NRs; however, when the rods are free of major defects, theoretical strengths are obtainable. Indeed, in the bending mode, defect-free SiC NRs now appear to be the strongest material known. We believe that by using this measurement technique as a critical test, it should be possible to optimize synthetic conditions (16) to produce near defect-free SiC NR samples that exhibit maximum strength values.

These strength results indicate that SiC NRs, despite their smaller E values, should be a better reinforcing material in some composite structures than carbon nanotubes. In particular, we suggest that the SiC NRs should be seriously considered for producing very high strength ceramic composites in which the SiC NRs are randomly dispersed in the ceramic matrix (40). A similarly structured ceramic composite fabricated with nanotubes may have inferior properties because of the large reduction in nanotube stiffness after buckling.

Carbon nanotubes should, however, be considered for other types of mechanical applications. In particular, the elastic buckling exhibited by carbon nanotubes makes them exceedingly tough materials. We quantified the toughness or energy-absorbing capability of the MWNTs by integrating the measured F-d curves (Fig. 4). A lower bound (that is, to the point where the AFM tip passes over the tube) on the stored strain energy for 30-nm-diameter nanotubes is 100 keV. This lower bound is on the order of 5 to 10 times the strain energy stored in comparable diameter SiC NRs before fracture. Hence, the ability of carbon nanotubes to elastically sustain loads at large deflection angles enables them to store or absorb considerable energy. One obvious application of this unique energy-absorbing capability of carbon nanotubes would be in armor, although a suitable matrix must be chosen to exploit these properties in a macroscopic article. Clearly, carbon nanotubes and carbide NRs are materials with great potential in mechanical applications.

REFERENCES AND NOTES

1. C. Herring and J. K. Galt, *Phys. Rev.* **85**, 1060 (1952).
2. W. W. Webb and W. D. Forgeng, *Acta Metall.* **6**, 462 (1958).
3. A. P. Levitt, in *Whisker Technology*, A. P. Levitt, Ed. (Wiley-Interscience, New York, 1970), pp.1–13.
4. R. L. Mehan and J. A. Herzog, in *ibid.*, pp.157–196.
5. C. C. Evans, *Whiskers* (Mills and Boon, London, 1972), pp. 46–65.
6. J. J. Petrovic, J. V. Milewski, D. L. Rohr, F. D. Gac, *J. Mater. Sci.* **20**, 1167 (1985); J. J. Petrovic and R. C. Hoover, *ibid.* **22**, 517 (1987).
7. N. H. Macmillan, *ibid.* **7**, 239 (1972).
8. B. I. Yakobson, C. J. Brabec, J. Bernholc, *Phys. Rev. Lett.* **76**, 2511 (1996).
9. S. Iijima, C. Brabec, A. Maiti, J. Bernholc, *J. Chem. Phys.* **104**, 2089 (1996).
10. C. F. Cornwell and L. T. Wille, *Solid State Commun.* **101**, 555 (1997).
11. T. W. Ebbesen and P. M. Ajayan, *Nature* **358**, 220 (1992).
12. J. F. Despres, E. Daguerre, K. Lafdi, *Carbon* **33**, 87 (1995).
13. S. Subramoney, R. S. Ruoff, R. Laduca, S. Awadalla, K. Parvin, in *Proceedings of the Symposium on Recent Advances in the Chemistry and Physics of Fullerenes and Related Materials*, Electrochemical Society, Reno, NV, 16 to 21 May 1995, R. S. Ruoff and K. M. Kadish, Eds. (Electrochemical Society, Pennington, NJ, 1995), pp. 557–562.
14. D. T. Colbert *et al.*, *Science* **266**, 1218 (1994).
15. T. Guo, P. Nikolaev, A. Thess, D. T. Colbert, R. E. Smalley, *Chem. Phys. Lett.* **243**, 49 (1995); A. Thess *et al.*, *Science* **273**, 483 (1996).
16. H. Dai, E. W. Wong, Y. Z. Lu, S. Fan, C. M. Lieber, *Nature* **375**, 769 (1995).
17. P. Yang and C. M. Lieber, *Science* **273**, 1836 (1996).
18. R. H. Kelsey, in (3), pp. 135–156.
19. M. M. J. Treacy, T. W. Ebbesen, J. M. Gibson, *Nature* **381**, 678 (1996).
20. N. Osakabe, K. Harada, M. I. Lutwyche, H. Kasai, A. Tonomura, *Appl. Phys. Lett.* **70**, 940 (1997).
21. H. Dai, E. W. Wong, C. M. Lieber, *Science* **272**, 523 (1996).
22. P. E. Sheehan and C. M. Lieber, *Nanotechnology* **7**, 236 (1996).
23. The lateral load causes the nanobeam to exert an upward force on the cantilever-tip assembly. When this upward force exceeds the applied normal load, the tip passes over the nanobeam. The applied normal load can be varied in our experiments to control the degree to which the nanobeams are deflected.
24. F. P. Beer and E. R. Johnston Jr., *Mechanics of Materials* (McGraw-Hill, New York, 1992), p. 486.
25. The boundary conditions are $y(x = 0) = y'(x = 0) = 0$ and $y''(x = L) = y'''(x = L) = 0$, where $x = L$ corresponds to the end of the beam. Furthermore, the force P is only applied at the point a.
26. Linearized plots of the data, $k^{-1/3}$ versus x, have a slope of $[4/(3\pi r^4 E)]$ and intercept of $[4/(3\pi r^4 E)]^{1/3}\Delta$, where Δ corresponds to deviation in the pinning point from the edge of the SiO pad. The corrections to the pinning point from this analysis are up to 50 nm.
27. It is assumed that bulk SiC dominates the measured E values in the 10- to 30-nm-diameter NRs probed in our studies. This assumption may break down for NRs that oxidize to SiO_x at the surface because the oxide has a smaller modulus than SiC; the near-surface region of the rods makes a large contribution to measured results because $I \propto r^4$.
28. The observed deformation (Fig. 2A) corresponds to the NR bending and not to the motion of the pinned portion of the NR under the SiO pad. First, if the NR was rigid and the measured displacement occurred under the SiO pad, then the deformation could not be elastic (as observed) because bonds would be broken at the SiO-MoS$_2$, SiO-NR, and NR-MoS$_2$ interfaces (resulting in energy dissipation). Second, motion of the NR underneath the thin SiO pinning film would change the topography of the pad. Our AFM measurements show no evidence of this.
29. W. R. L. Lambrecht, B. Segall, M. Methfessel, M. van Schilfgaarde, *Phys. Rev. B* **44**, 3685 (1991).
30. The location at which the lateral force begins to increase linearly with displacement differs in some of the horizontal scans of Fig. 3. Comparison of F-d data recorded for forward and reverse scans indicates strongly that these deviations are due to a small component of friction at the nanotube-MoS$_2$ interface.

31. The MWNT E values were calculated with the assumption that the nanotubes are solid cylinders. TEM imaging of our MWNTs showed that they have hollow cores with diameters ≤ 2 nm. Because the moment of inertia scales as r^4, this assumption produces only a very small error on the order of 0.01%.

32. O. L. Blakslee, D. G. Proctor, E. J. Seldin, G. B. Spence, T. Weng, *J. Appl. Phys.* **41**, 3373 (1970).

33. D. H. Robertson, D. W. Brenner, J. W. Mintmire, *Phys. Rev. B* **45**, 12592 (1992).

34. G. Overney, W. Zhong, D. Tomanek, *Z. Phys. D* **27**, 93 (1993).

35. R. S. Ruoff and D. C. Lorentz, *Carbon* **33**, 925 (1995).

36. J. P. Lu, *Phys. Rev. Lett.* **79**, 1297 (1997).

37. The discontinuity in *F-d* is not due to a discontinuity in the topography. First, high-resolution images demonstrate that the MoS_2 substrate is atomically flat in the region where the force discontinuity is observed. Furthermore, the topographic signal, which was recorded at the same time as *F*, is constant across the region of force discontinuity.

38. Mechanical deformation of metal whiskers ultimately leads to a decrease in the initial linear (elastic) *F-d* behavior. This decrease is, however, due to plastic deformations (4).

39. D. Hull and T. W. Clyne, *An Introduction to Composite Materials* (Cambridge Univ. Press, Cambridge, 1996).

40. The bending strength is relevant to composites formed with randomly oriented nanotubes or NRs. In a composite made with oriented nanotubes or NRs, the tensile and compressive strengths should also be considered. The tensile and bending strengths are comparable for SiC whiskers (6, 7) and are also expected to be similar for SiC NRs. The tensile strength of a carbon nanotube is, however, expected to be substantially larger than the nanotube bending strength and the strength of SiC NRs.

41. We thank J. W. Hutchinson and F. Spaepen for helpful discussions and S. Shepard for assistance with SiO deposition. C.M.L. acknowledges partial support of this work by the NSF Division of Materials Research and the Air Force Office of Scientific Research.

Enhancement of Protein Crystal Nucleation by Critical Density Fluctuations

Pieter Rein ten Wolde and Daan Frenkel*

Numerical simulations of homogeneous crystal nucleation with a model for globular proteins with short-range attractive interactions showed that the presence of a metastable fluid-fluid critical point drastically changes the pathway for the formation of a crystal nucleus. Close to this critical point, the free-energy barrier for crystal nucleation is strongly reduced and hence, the crystal nucleation rate increases by many orders of magnitude. Because the location of the metastable critical point can be controlled by changing the composition of the solvent, the present work suggests a systematic approach to promote protein crystallization.

As a result of rapid developments in biotechnology, there has been an explosive growth in the number of proteins that can be isolated. However, the determination of the three-dimensional structures of proteins by x-ray crystallography remains a time-consuming process. One bottleneck is the difficulty of growing protein crystals good enough for analysis. In his book on this subject, McPherson wrote, "The problem of crystallization is less approachable from a classical analytical standpoint, contains a substantial component of trial and error, and draws more from the collective experience of the past century. . . . It is much like prospecting for gold" (1, p. 6). The experiments clearly indicate that the success of protein crystallization depends sensitively on the physical conditions of the initial solution (1, 2). It is therefore crucial to understand the physical factors that determine whether a given solution is likely to produce good crystals.

Studies have shown that not just the strength but also the range of the interactions between protein molecules is crucial for crystal nucleation. In 1994, George and Wilson (3) demonstrated that the success of crystallization appears to correlate with the value of B_2, the second osmotic virial coefficient of the protein solution.

The second virial coefficient describes the lowest order correction to the van't Hoff law for the osmotic pressure Π:

$$\Pi/\rho k_B T = 1 + B_2 \rho + (\text{terms of order } \rho^2) \tag{1}$$

where ρ is the number density of the dissolved molecules, k_B is Boltzmann's constant, and T is the absolute temperature. For macromolecules, B_2 can be determined from static light-scattering experiments (4). Its value depends on the effective interaction between a pair of macromolecules in solution (5).

George and Wilson measured B_2 for a number of proteins in various solvents. They found that for those solvent conditions that are known to promote crystallization, B_2 was restricted to a narrow range of small negative values. For large positive values of B_2, crystallization did not occur at all, whereas for large negative values of B_2, protein aggregation rather than crystallization took place.

Rosenbaum, Zamora, and Zukoski (6, 7) established a link between the work of George and Wilson and earlier studies of the phase behavior of spherical, uncharged colloids (8–11). Since the theoretical work of Gast, Russel, and Hall (8), it has been known that the range of attraction between

spherical colloids has a drastic effect on the appearance of the phase diagram. If the range of attraction is long in comparison with the diameter of the colloids, the phase diagram of the colloidal suspension resembles that of an atomic substance, such as argon. Depending on the temperature and density of the suspension, the colloids can occur in three phases (Fig. 1A): a dilute colloidal fluid (analogous to the vapor phase), a dense colloidal fluid (analogous to the liquid phase), and a colloidal crystal phase. However, when the range of the attraction is reduced, the fluid-fluid critical point moves toward the triple point, where the solid coexists with the dilute and dense fluid phases. If the range of attraction is made even shorter (less than 25% of the colloid diameter), two stable phases remain, one fluid and one solid (Fig. 1B). However, the fluid-fluid coexistence curve survives in the metastable regime below the fluid-solid coexistence curve (Fig. 1B). This is indeed found in experiments (11, 12) and simulations (10). This observation is relevant for solutions of globular proteins, because they often have short-range attractive interactions. A series of studies (13–15) showed that the phase diagram of a variety of proteins is of the kind shown in Fig. 1B. Moreover, the range of the effective interactions between proteins can be changed by the addition of nonadsorbing polymer (such as polyethylene glycol) (11, 16) or by changing the pH or salt concentration of the solvent (1, 2).

Rosenbaum, Zamora, and Zukoski (6, 7) observed that the conditions under which a large number of globular proteins can be made to crystallize map onto a narrow temperature range, or more precisely, a narrow range in the value of the osmotic second virial coefficient of the computed fluid-solid coexistence curve of colloids with short-range attraction (10). Several authors had already noted that a similar crystallization window exists for colloidal suspensions (17). Here our aim was to use simulation to gain insight into the physical mechanism responsible for the en-

FOM Institute for Atomic and Molecular Physics, Kruislaan 407, 1098 SJ Amsterdam, Netherlands.

*To whom correspondence should be addressed.